Photoacoustics 9 (2018) 10–20

Contents lists available at ScienceDirect

Photoacoustics

journal homepage: www.elsevier.com/locate/pacs

Research article

The characterization of an economic and portable LED-based photoacoustic imaging system to facilitate molecular imaging

Ali Hariri[a], Jeanne Lemaster[a], Junxin Wang[a], AnanthaKrishnan S. Jeevarathinam[a], Daniel L. Chao[b], Jesse V. Jokerst[a,c,d,*]

[a] Department of NanoEngineering, University of California, San Diego, 9500 Gilman Drive, La Jolla, CA 92092, United States
[b] Shiley Eye Institute, Department of Ophthalmology, University of California, San Diego, 9500 Gilman Drive, La Jolla, CA 92092, United States
[c] Materials Science and Engineering Program, University of California, San Diego, 9500 Gilman Drive, La Jolla, CA 92092, United States
[d] Department of Radiology, University of California, San Diego, 9500 Gilman Drive, La Jolla, CA 92092, United States

ARTICLE INFO

Article history:
Received 27 April 2017
Received in revised form 6 November 2017
Accepted 19 November 2017
Available online 26 November 2017

Keywords:
Portable photoacoustic imaging
LED
Optoacoustic imaging
Molecular imaging

ABSTRACT

Photoacoustic imaging (PAI) is a non-invasive, high-resolution hybrid imaging modality that combines optical excitation and ultrasound detection. PAI can image endogenous chromophores (melanin, hemoglobin, etc.) and exogenous contrast agents in different medical applications. However, most current equipment uses sophisticated and complicated OPO lasers with tuning and stability features inconsistent with broad clinical deployment. As the number of applications of PAI in medicine increases, there is an urgent need to make the imaging equipment more compact, portable, and affordable. Here, portable light emitting diode – based photoacoustic imaging (PLED-PAI) was introduced and characterized in terms of system specifications, light source characterizations, photoacoustic spatial/temporal resolution, and penetration. The system uses two LED arrays attached to the sides of a conventional ultrasound transducer. The LED pulse repetition rate is tunable between 1 K Hz, 2 K Hz, 3 K Hz, and 4 K Hz. The axial resolution was 0.268 mm, and the lateral resolution was between 0.55 and 0.59 mm. The system could detect optical absorber (pencil lead) at a depth of 3.2 cm and the detection limits of indocyanine green (ICG) and methylene blue (MB) were 9 μM and 0.78 mM. *In vivo* imaging of labeled human mesenchymal stem cells was achieved to confirm compatibility with small animal imaging. The characterization we report here may have value to other groups evaluating commercially available photoacoustic imaging equipment.

1. Introduction

Photoacoustic imaging (PAI) is a non-invasive, and non-ionizing imaging modality based on optical absorption/excitation and ultrasound detection [1]. It offers the contrast and spectral behavior of optical imaging combined with the high penetration depth and spatial resolution of acoustic imaging due to weak ultrasound scattering in biological tissue. In PAI, tissue is illuminated by a nanosecond laser pulse. Endogenous or exogenous molecules will absorb this incident energy to produce a fast local temperature increase; acoustic waves then propagate inside the tissue due to thermal expansion. Wideband ultrasound transducers can detect photoacoustic signal via *trans*-abdominal [2] or intra-vascular [3] settings, and the combination of PAI with ultrasound can offer functional details as well as anatomical and structural information [4,5]. This high-resolution modality has been used to image endogenous chromophores (melanin, hemoglobin, etc.) and exogenous contrast agents [6] in different medical applications including molecular imaging [7–10], oncology [11,12], ophthalmology [13,14], cardiology [15], and neurology [16,17].

When selecting a photoacoustic excitation source, one should consider the pulse width of the light source, the pulse energy, repetition rate, wavelength, and the spectral width of the source. These should be compared to the absorption behavior of the target tissue/contrast agent. High energy Nd:YAG lasers are the most common PAI excitation sources. These lasers generate 4–7 ns pulses with mJ energy levels. The repetition rates are limited to between 10 and 30 Hz. NIR optical parametric oscillator (OPO) or dye lasers are the most common [18]. However, dual modality imaging systems (ultrasound/photoacoustic) with these lasers are bulky, expensive, and suffer from wavelength and power intensity

* Corresponding author at: Department of NanoEngineering, University of California, San Diego, 9500 Gilman Drive, La Jolla, CA 92092, United States.
E-mail address: jjokerst@ucsd.edu (J.V. Jokerst).

https://doi.org/10.1016/j.pacs.2017.11.001

fluctuations. These systems typically use a laser enclosure system to shield the operator from the incident irradiation, but this is cumbersome and prevents the operator from directly interacting with the sample or subject. While miniaturized OPOs offer a small footprint [19,20], they remain delicate and expensive and require regular maintenance.

To overcome these limitations, pulse laser diodes (PLD) have been utilized as an illumination light source in different PAI configurations such as optical resolution microscopy (OR-PAM) [21,22] and photoacoustic computed tomography (PACT) [23,24]. For example, Daoudi et al. [25], developed a compact and ergonomic handheld dual modality (ultrasound/photoacoustic) probe using PLD with axial resolution of 0.28 mm and lateral resolution between 0.4 mm and 0.6 mm as well as considerable penetration depths (15 mm). More recently, light emitting diodes (LEDs) have also been used for PAI [26]. These inexpensive, compact, and multi-wavelength LED-based designs were shown in Allen et al. [27], and Adachi et al. [28] for photoacoustic microscopy (PAM).

Indeed, LEDs solve many issues in the clinical translation of PAI. Most importantly, they offer a significant reduction in cost, are significantly more stable than OPO-based systems, and take up only a fraction of the space. This stability and reduced footprint makes LED-based systems portable [29]. Furthermore, LEDs do not have to be in a light-tight enclosure, which can restrict many clinical procedures. There are several clinical examples were this would be useful including the gastrointestinal imaging of Zhang et al. [30] and the brain resection work of Kircher et al. [31].

In addition, we [32] and others [33,34] have recently utilized photoacoustic imaging techniques for real-time monitoring of therapeutics or disease biomarkers such as circulating tumor cells, heparin, or lithium [35,36]. These applications are ideally suited for LED-based illumination because they need low cost and portable excitation sources. They perturb only the first few millimeters of tissue, and thus do not require the high energy of OPO-based lasers. Thus, this work with wearable photoacoustic imaging applications motivated us to pursue a commercially available LED-based photoacoustic scanner.

In this study, we characterize a commercially available LED-based photoacoustic system, defined here as a portable LED-based photoacoustic imaging (PLED-PAI). In the following sections, we describe system specification, light source characterization, photoacoustic spatial/temporal resolution, and penetration depth. We then report this system's performance with common exogenous photoacoustic contrast agents including pilot rodent *in vivo* applications.

2. Methods and materials

2.1. System description

The PLED-PAI consists of an optical path and an acoustic path and was purchased from Prexion Corporation. (Tokyo, Japan; Fig. 1). High density, high power light emitting diodes (Prexion Corporation, Tokyo, Japan) are used as an excitation source. Two LED arrays are attached to either side of an ultrasound transducer. Each LED array includes 4 rows of 36 single embedded LEDs. Each LED array has 2 rows with 850 nm excitation and 2 rows with 690 nm excitation. One array is placed on each side of the transducer for four rows at each wavelength (Fig. 1D). Each LED array head has dimension of 12.4 mm (height), 86.5 mm (length), and 10.2 mm (width). The LED pulse width can be changed from 50 ns – 150 ns with a 5 ns step size. The LED pulse repetition rate is tunable between 1 K Hz, 2 K Hz, 3 K Hz, and 4 K Hz; the temporal resolution is dependent on choice of repetition rate. Photoacoustic signals are generated after each LED pulse. The 128 elements of the linear array transducer detect the photoacoustic signal in parallel

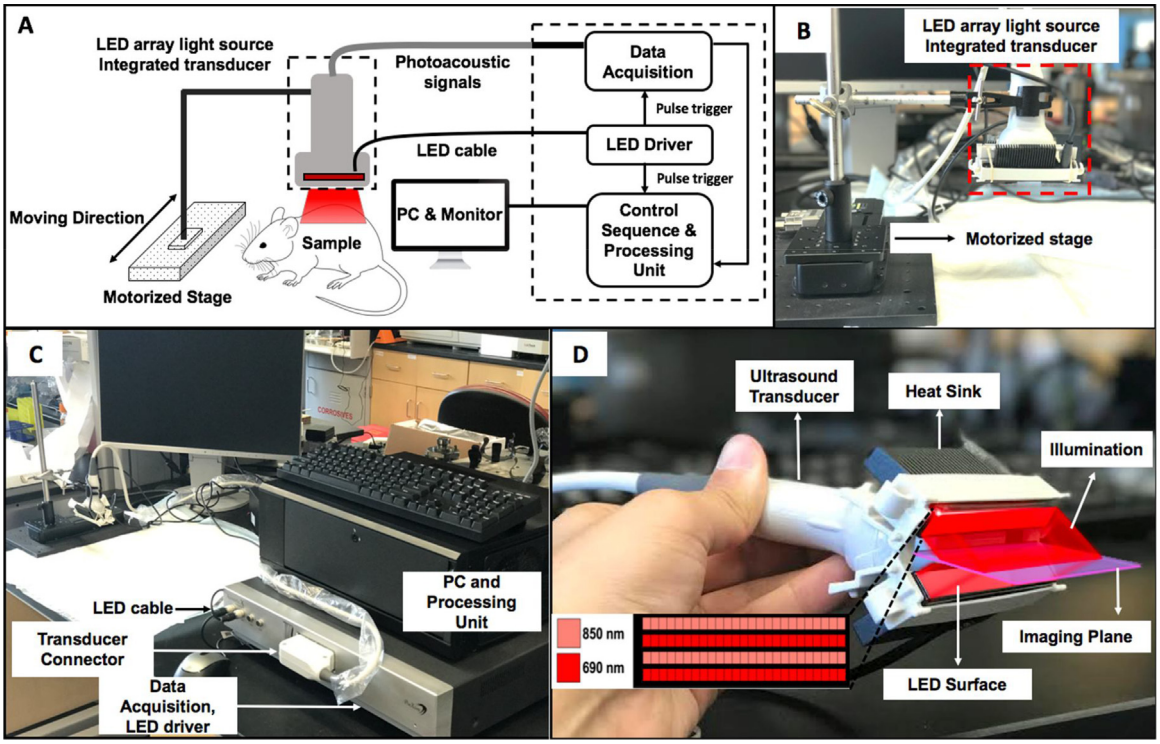

Fig. 1. Schematic and photograph of LED-based photoacoustic system. A) Schematic of the PAI system using LED array light source. B) Photograph of PLED-PAI probe associated with motorized stage. C) Whole imaging setup includes PC and processing unit, data acquisition, LED driver, ultrasound transducer, LED light source, and motorized stage. D) PLED-PAI probe with imaging plane and illumination source are shown schematically. LED array design is also shown in the inset—there were alternating rows of LEDs with different wavelengths.

and this reconstructs one frame. The frame rate in PLED-PAI is equal to the LED repetition rate because it has parallel acquisition channels in this system.

LED systems have lower power, and averaging is used to minimize noise. This affects the frame rate. There are a defined number of averages that change as a function of LED pulse repetition rate. In turn, these averaging options define the frame rate and temporal resolution. Options include: 1 K Hz (32, 64, 96, 160, 320, 640, 1600, 3200, and 6400 averages), 2 K Hz (64, 128, 192, 320, 640, 1280, 3200, 6400, and 12800 averages), 3 K Hz (128, 192, 320, 640, 1280, 3200, 6400, and 12800 averages), and 4 K Hz (128, 256, 384, 640, 1280, 2650, 6400, 12800, and 25600 averages). Therefore, the PLED-PAI can have frame rates of 30 Hz, 15 Hz, 10 Hz, 6 Hz, 3 Hz, 1.5 Hz, 0.6 Hz, 0.3 Hz, and 0.15 Hz. There are different methods rather than averaging to minimize the noise. Golay codes [37], empirical mode decomposition (EMD) [38], wavelet-based methods, and Wiener deconvolution have been applied to low SNR photoacoustic and are reported in the literature [39,40].

The acoustic path uses an ultrasound pulse/receive linear array transducer with 128 channels and central frequency of 10 MHz with bandwidth of 80.9%. (PreXion Corporation, Tokyo, Japan). Each element is 3.5 mm long with a pitch of 0.3 mm. An acoustic lens focuses the ultrasound at ~15 mm. The maximum ultrasound detection depth is 38 mm. The data acquisition unit has a dynamic range of 16 bits with 1024 samples for each element. The sampling rates of the photoacoustic and ultrasound modalities are 40 MHz and 20 MHz, respectively. The LED driver triggers and synchronizes the illumination and ultrasound detection (Fig. 1A). The photoacoustic signals are generated and stored after each LED pulse. B-mode photoacoustic and ultrasound images are reconstructed using a delay-and-sum (DAS) [41] and Fourier transform analysis (FTA) [42]. The transducer can be scanned in one direction to acquire three-dimensional (3D) data.

2.2. LED beam characterization

2.2.1. LED beam profile

To evaluate the excitation sources, parallel lines were printed 2 mm apart on transparency films and placed inside a 1% agar phantom (Fig. 2A). The PLED-PAI was placed 2 cm from the lines. Thus, identical absorbers with the same thickness values at the same depth were used to characterize the LED light source based on the photoacoustic signal that they produce. The probe scans in one direction using a motorized translation stage (OptoSigma Corporation, CA, USA) for 10 mm. A maximum intensity projection (MIP) was used to reconstruct the 3D image. To analyze each line in the MIP, we converted the MIP image to an 8-bit TIFF file using ImageJ 1.48 v [43]. Ten different regions of interest (ROI) were used to measure the accumulative photoacoustic intensity on each line.

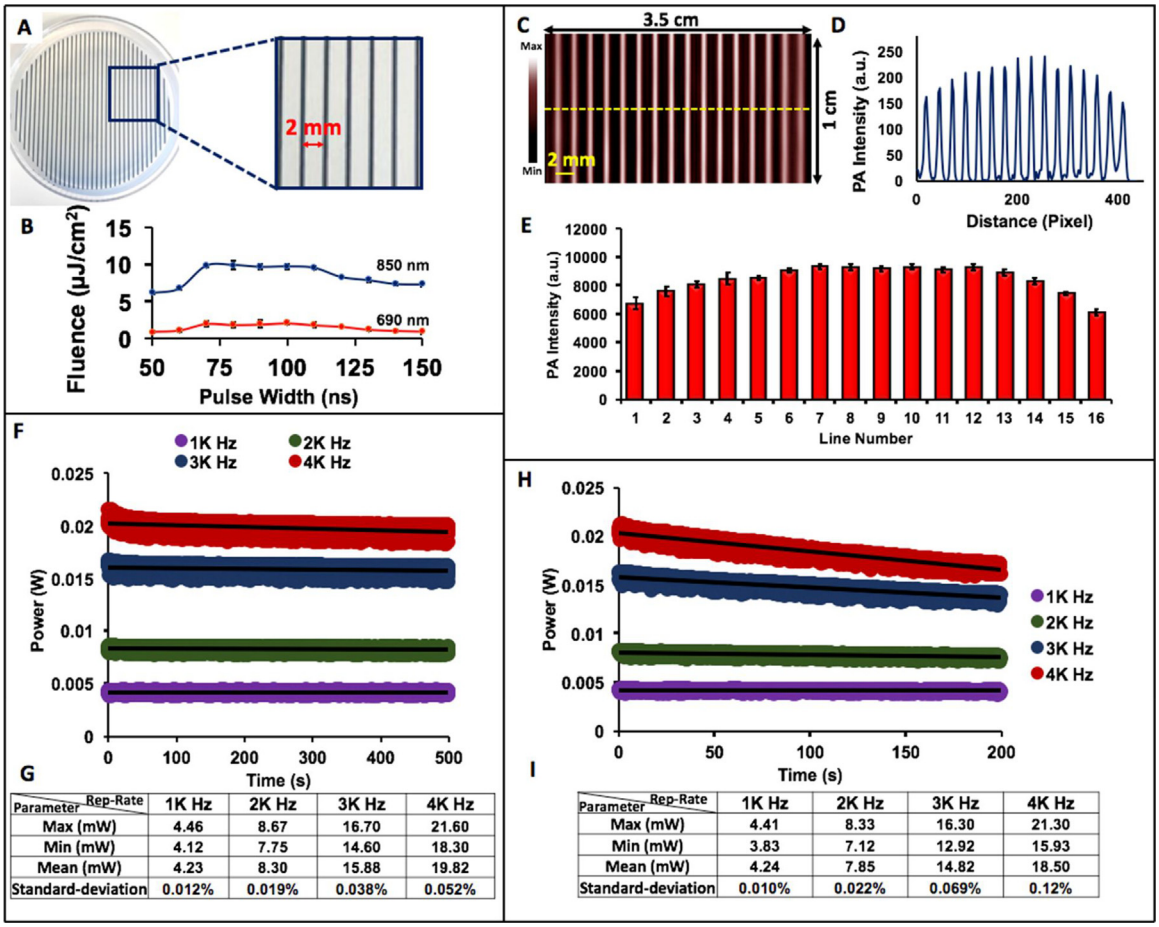

Parameter / Rep-Rate	1K Hz	2K Hz	3K Hz	4K Hz
Max (mW)	4.46	8.67	16.70	21.60
Min (mW)	4.12	7.75	14.60	18.30
Mean (mW)	4.23	8.30	15.88	19.82
Standard-deviation	0.012%	0.019%	0.038%	0.052%

Parameter / Rep-Rate	1K Hz	2K Hz	3K Hz	4K Hz
Max (mW)	4.41	8.33	16.30	21.30
Min (mW)	3.83	7.12	12.92	15.93
Mean (mW)	4.24	7.85	14.82	18.50
Standard-deviation	0.010%	0.022%	0.069%	0.12%

Fig. 2. LED beam characterizations of PLED-PAI system. A) Parallel lines were printed on transparency film and placed inside 1% agar. The distance between the lines is 2 mm. B) LED fluence per pulse versus pulse width for 690 and 850 nm. C) MIP image for sixteen parallel lines with a scan size of 10 mm. D) The line profile along the dotted line in C. E) Statistical analysis of each line and the averaged PA intensity along all sixteen lines. Error bars show standard deviation between different ROIs in each printed line. F) LED power stability (in different repetition rates) versus time when PLED-PAI is placed inside the water. G) LED power statistical parameters when PLED-PAI is in water for 500 s. H) LED power stability (in different repetition rates) versus time when PLED-PAI is placed inside the air. I) LED power statistical parameters for PLED-PAI in air for 200 s.

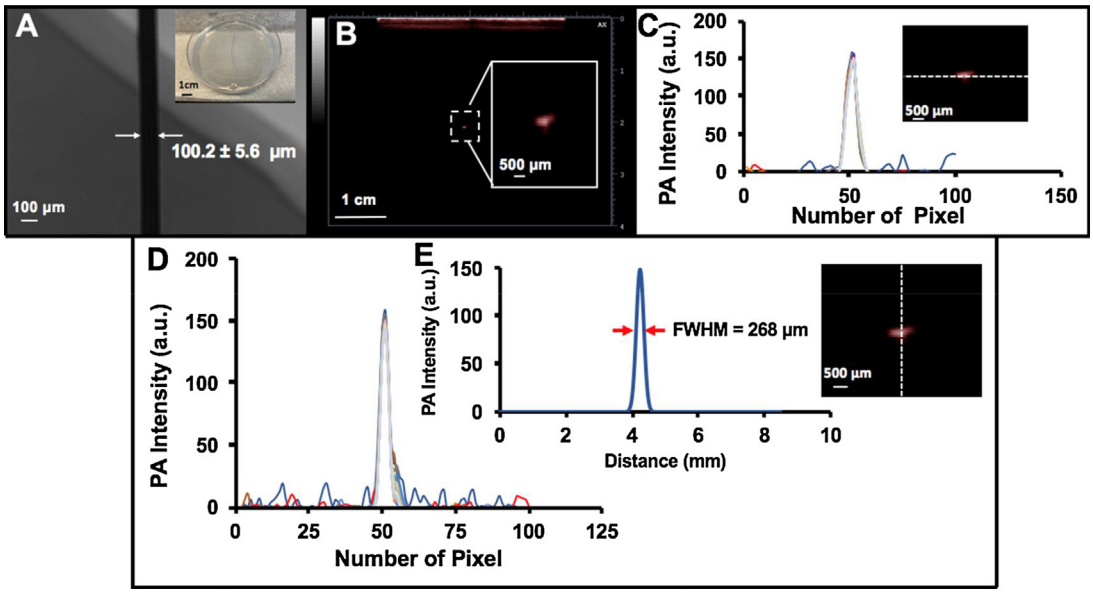

Fig. 3. Axial resolution by measuring photoacoustic point spread function using a human black hair. A) Photograph and bright field microscopy image of black hair inside 1% agar phantom. The thickness of the hair is 100.1 ± 5.6 μm. B) Photoacoustic image of hair. Image size is 3.5 cm × 4 cm. The image is reconstructed using the FTA algorithm. C) Lateral profile along dotted line for all conditions with different colors (1 K Hz (32, 64, 96, 160, 320, 640, 1600, 3200, and 6400 averages), 2 K Hz (64, 128, 192, 320, 640, 1280, 3200, 6400, and 12800 averages), 3 K Hz (128, 192, 320, 640, 1280, 3200, 6400, and 12800 averages), and 4 K Hz (128, 256, 384, 640, 1280, 2650, 6400, 12800, and 25600 averages). There is no significant difference in lateral profile in this phantom as a function of repetition rate or averages. D) Axial profile for all conditions with different colors. E) Fitted Gaussian distribution on the axial profile with measured FWHM. Axial resolution is 268 μm.

2.2.2. LED power and stability

To measure the LED stability, a photodiode sensor was positioned 5 mm from the LED sources (small aperture (1 cm) photodiode sensor (S120C, Thorlabs Inc., USA)). We studied the LEDs at four different repetition rates (1, 2, 3, and 4 K Hz) while immersed in water (for 500 s) and air (for 200 s). The temperature of the LED surface and the heat sink was recorded. The power delivered from the LED arrays was calculated using a standard photodiode sensor (S120C, Thorlabs Inc., USA) at 690 and 850 nm.

2.3. Photoacoustic spatial resolution

2.3.1. Axial resolution

To measure the axial resolution, a black human hair was embedded inside a 1% agar phantom. A bright field microscopy imaging system (Life Technologies Inc., Ca, USA) was used to calculate the hair diameter (100.15 ± 5.60 μm) (Fig. 3A). The hair was positioned 2 cm below the transducer. Photoacoustic images were reconstructed using FTA methods for all conditions (1 K Hz (32, 64, 96, 160, 320, 640, 1600, 3200, and 6400 averages), 2 K Hz (64, 128, 192, 320, 640, 1280, 3200, 6400, and 12800 averages), 3 K Hz (128, 192, 320, 640, 1280, 3200, 6400, and 12800 averages), and 4 K Hz (128, 256, 384, 640, 1280, 2650, 6400, 12800, and 25600 averages)). The axial profile was plotted and fitted to a Gaussian distribution. The full width half maximum (FWHM) was calculated using MATLAB software (MathWorks Inc.).

2.3.2. Lateral resolution

To characterize the lateral resolution, parallel lines (150 μm wide) with different distances (from 1.1 mm to 0.55 mm) were printed on a transparency film (Fig. 4A). After placing the transparency films at various distances inside 1% agar, photoacoustic images were acquired using PLED-PAI with FTA image reconstruction. Bright field microscopy was used to measure the accurate spacing between lines, and PAI line profiles were used to measure the lateral resolution.

2.4. Photoacoustic penetration depth

To evaluate the PLED-PAI system penetration depth, chicken breast tissue was used as a scattering media. A single pencil lead (0.5 mm HB, Newell Rubbermaid, Inc., IL, USA) was inserted inside

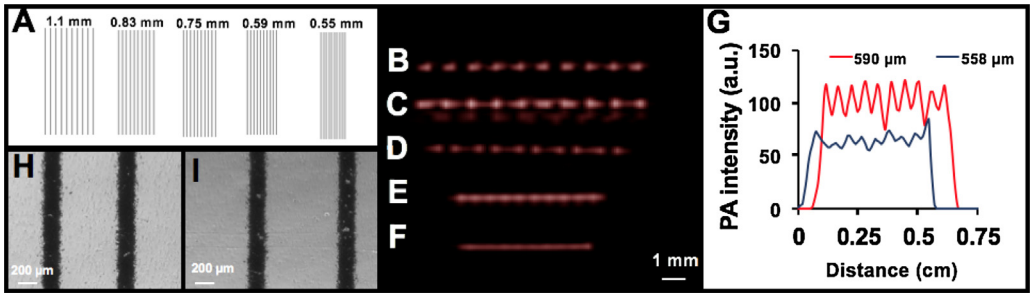

Fig. 4. Lateral resolution measurement of LED-based photoacoustic imaging system. A) Parallel lines with various spacing (1.1 mm, 0.83 mm, 0.75 mm, 0.59, and 0.55 mm) are printed on transparency film and placed inside 1% agar phantom. B) Photoacoustic image for 1.1 mm spacing between lines. C) 0.83 mm spacing. D) 0.75 mm. E) 0.59 mm. F) 0.55 mm. G) Lateral profile for two different samples (0.59 mm and 0.55 mm). This plot shows that LED-based photoacoustic imaging can distinguish lines when there is 0.59 mm spacing between lines. The 0.55 mm spacing cannot be resolved by this imaging system. H) Bright field microscopy image for 0.59 mm spacing. I) Bright field microscopy image for 0.75 mm spacing.

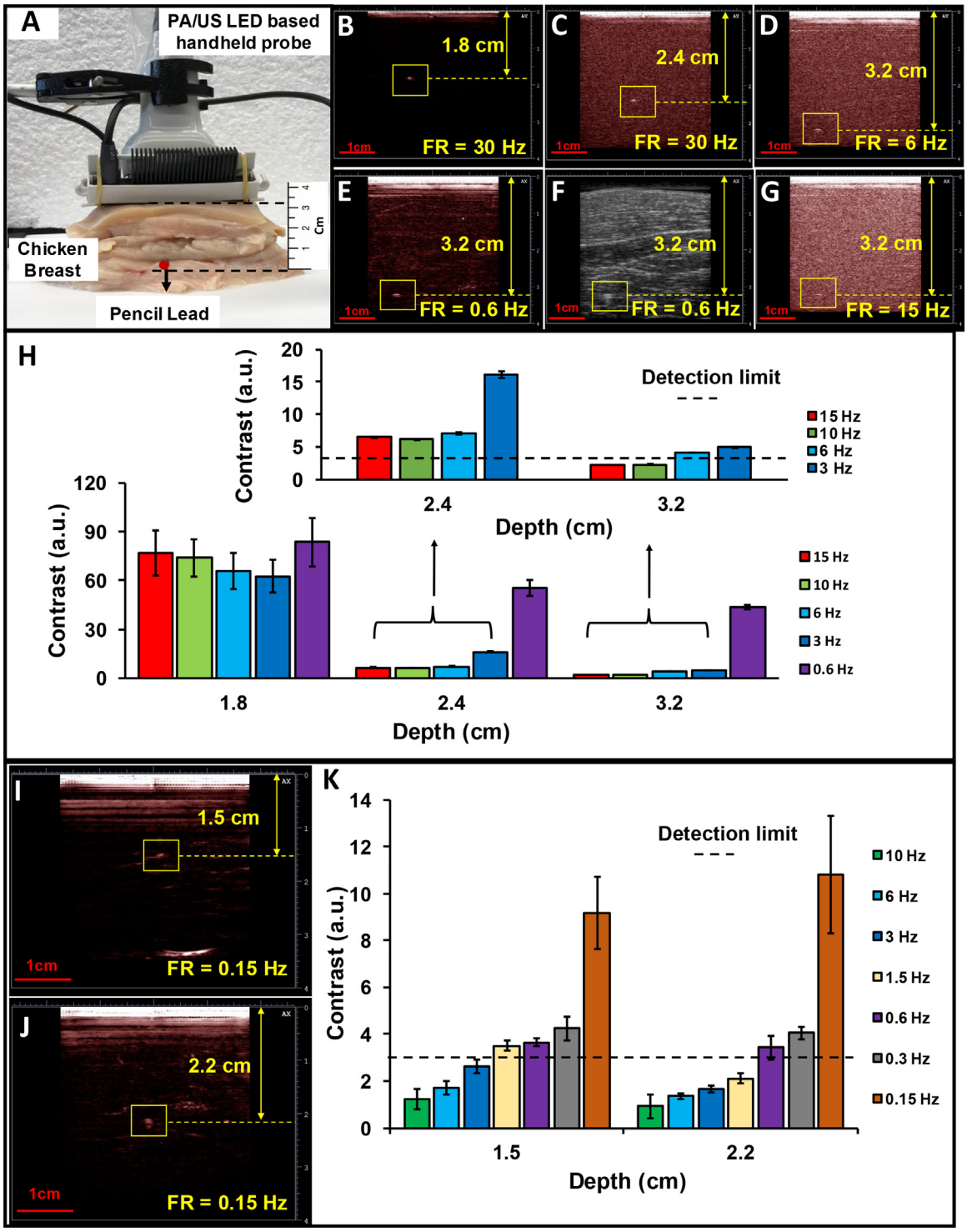

Fig. 5. Penetration depth measurement of PLED-PAI. A) Experimental configuration includes chicken breast tissue with pencil lead 3.2 cm deep. B) Photoacoustic image of pencil lead 1.8 cm deep with a frame rate (FR) of 30 Hz C) Depth of 2.4 cm when FR = 30 Hz. D) Depth of 3.2 cm when FR = 6 Hz. By increasing the depth, the photoacoustic system acquires more averages (decrease the frame rate) to improve SNR. E) Depth of 3.2 cm when FR = 0.6 Hz F) B-mode ultrasound image of pencil lead 3.2 cm deep with a frame rate of 0.6 Hz. The ultrasound resolution at 10 MHz does not clearly discriminate the target. G) Photoacoustic image of pencil lead 3.2 cm deep when FR = 15 Hz. The SNR decreases by increasing the frame rate. Object is poorly defined with low contrast. H) Signal to background noise as a function of depth and frame rate. Panels I-K are blood samples below chicken breast tissue. Panel I is a frame rate of 0.15 Hz J) Photoacoustic image of blood sample 2.2 cm deep when frame rate of 0.15 Hz K). Signal-to-background noise as a function of depth and frame rate for blood sample inside the chicken breast. If the contrast is lower than the detection limit (S/N < 3), then the specimen cannot be detected.

chicken breast as an optical absorber at different distances from the transducer surface (Fig. 5A) [44]; 850 nm LEDs were used as the illumination source. This sample was scanned at different depths (1.8 cm, 2.4 cm, and 3.2 cm) with different frame rates (30 Hz, 15 Hz, 10 Hz, 6 Hz, 3 Hz, 1.5 Hz, 0.6 Hz, 0.3 Hz, and 0.15 Hz). To have a more realistic absorber, ten μL blood were placed inside Teflon light wall tubes (Component Supply Company, FL, USA). These were scanned at a depth of 1.5 and 2.2 cm with different

frame rates. Contrast is defined as a ratio of photoacoustic (S) and background noise (N) intensity in the photoacoustic image ($C = \frac{S}{N}$). The photoacoustic images are reconstructed using FTA methods.

To measure the signal and the noise, a window of 4 pixels × 4 pixels was placed where the image has a high photoacoustic intensity, and the mean intensity of the pixels in this 4 × 4 area was calculated. The same procedure was utilized to measure the background noise intensity: a 4 pixel × 4 pixel window was positioned 2 mm away from the object, and the background noise intensity mean values are measured—contrast values above 3 are considered recognizable (Fig. 5G).

2.5. Exogenous contrast agent in photoacoustic imaging

Indocyanine green (ICG) (Chem-Impex Int'l Inc., IL, USA), methylene blue (MB) (Fisher Science Education Inc., PA, USA), and 1,1′-dioctadecyl-3,3,3′,3′-tetramethylindo-tricarbocyanine iodide (DiR) (Biotium Inc., CA, USA) were purchased and dissolved in deionized (DI) water (ICG and MB) or dimethyl sulfoxide (DMSO) (DiR). Ten μL of each solution (36 μM, 18 μM, and 9 μM ICG; 1.5 mM, 0.75 mM, and 0.37 mM MB; and 136 μM, 68 μM, and 136 μM DiR) were used for photoacoustic imaging. Samples were placed inside Teflon light wall tubes (Component Supply Company, FL, USA) and positioned under 1 cm layer of 2% intralipid (20%, emulsion, Sigma-Aldrich Co, MO, USA) mixed with agar. Water or DMSO served as controls. ICG and DiR used 850 nm excitation, and MB used 690 nm excitation. All samples were scanned at a depth of 10 mm from the transducer, and a MIP was used to reconstruct the images. We repeated this at higher concentrations (640 μM, 320 μM, and 160 μM ICG; 6 mM, 3 mM, and 1.5 mM MB; and 592 μM, 296 μM, and 148 μM DiR). ImageJ 1.48 v was used to do statistical analysis. Ten different regions of interest (ROI) were used to measure the average photoacoustic intensity for each sample.

2.6. In vivo *imaging using PLED-PAI*

All animal experiments were performed in compliance with the Institutional Animal Care and Use Committee established by University of California San Diego. Male mice were anesthetized with 2.5% isofluorane in oxygen at 1.5 L/min.

Poietics human mesenchymal stem cells (HMSCs; Lonza, PT-2501, NJ, USA) were grown in supplemented media (Lonza, PT-3001, NJ, USA) and seeded in a T75 flask at a concentration of 5000 cells/cm^2. Cells (400,000) were labeled with 9.8 mM DiR and incubated under standard conditions for 20 min. The HMSCs were washed with PBS to remove free nanoparticles and detached using TrypLE Express (Life Technologies Inc., Ca, USA). Then, 100 μL of three different materials such as only DiR (positive control), HMSC labeled with DiR (DiR @ HMSC), and HMSC (negative control) were subcutaneously injected on the spinal cord of male mice as an in-vivo experiment. B-mode photoacoustic/ultrasound images were reconstructed using the FTA algorithm.

3. Results and discussion

3.1. LED beam characterization

The beam characterization is divided into three parts: LED beam profile, illumination stability, and LED power. We first measured the consistency of the LED illumination power across the scanning area, i.e., the beam profile. Since 70 ns pulse width has almost the highest LED fluence for both 690 and 850 nm (Fig. 2B), we used this number as pulse width in all experiments. The temporal shape of excitation pulses and LED spectrums are shown in Supplementary Fig. 1S A, B, C. The power from the LED arrays at 690 nm and 850 nm with 70 ns as pulse width was measured to be 9.85 mW/cm^2 (2.6 μJ/cm^2 per pulse) and 31.55 mW/cm^2 (9 μJ/cm^2 per pulse), respectively for 4 K Hz repetition rate. Fig. 2C shows a maximum intensity projection (MIP) image of the printed transparency. Fig. 2D is a line profile along the dotted line on Fig. 2C. The photoacoustic intensities were averaged and are shown in Fig. 2E for each line. The error bars show the standard deviation along all intensities and ROIs. The average intensity of lines 3 through 14 (6 mm from either side of the transducer) is 18.43% higher than the values seen on the sides (Fig. 2D, E).

Next, the stability of the LED (850 nm) intensity was measured with a variation (between maximum power and minimum power) of 13.64%, 14.46%, 20.86%, and 25.35% for 1 K Hz, 2 K Hz, 3 K Hz, and 4 K Hz, respectively, in air (Fig. 2F). In water, the variation is 8.88%, 10.34%, 12.57%, and 15.27% for 1 K Hz, 2 K Hz, 3 K Hz, and 4 K Hz, respectively (Fig. 2H). The maximum (Max), minimum (Min), mean, and standard deviation (Std.) of the power in water (Fig. 2G) and air (Fig. 2I) are reported. There was a 14 °C temperature increase in the heatsink at a repetition rate of 4 K Hz; at 1 K Hz this was only 3.5 °C. For all conditions, we noticed a slight temperature increase (0.2-0.8 ° Celsius) on the actual LED surface.

The LED beam profile is a critical part of PAI systems, and light should be distributed equally on the sample. Different studies have reported different homogenized lateral illumination area. In the first report of handheld ultrasound/photoacoustic using a Q-switched laser, Niederhauser et al. [45] showed a homogenous illumination with a lateral size of 25 mm. Kolkman et al. [4] described a dual modality scanner with 20 mm as the lateral beam size by Nd:YAG laser. Daoudi et al. [25], reported 23 mm lateral beam size for their handheld probe integrating laser diode. The data in Fig. 2D, E show a homogenous beam over ~25 mm, which is comparable to the literature.

The temperature increase is due to the increased number of pulses—a higher repetition rate means a higher number of pulses in a specific time. In LEDs, the *p-n* junction diode emits light when activated, and LED light output varies as a function of this junction temperature. This local temperature increase is the main reason for LED power variations. Daoudi et al. [25] mentioned 5 to 10 ° in about 2 min of firing with repetition rate of 10 K Hz. Here, we noted that the PLED-PAI heatsink increased by 14 °C at a repetition rate of 4 K Hz; however, only a 0.2-0.8 Celsius temperature increase was observed on the LED surface.

3.2. Photoacoustic spatial resolution

Spatial resolution is important for imaging systems and is defined as the ability to distinguish two small high contrast objects positioned very close together. Fig. 3B shows the photoacoustic image of human hair inside agar phantom at a depth of 2 cm. The FWHM was calculated after preparing a Gaussian fit for axial resolution. This was defined as the axial resolution. Both lateral (Fig. 3C) and axial (Fig. 3D) profiles were analyzed for all conditions: 1 K Hz (32, 64, 96, 160, 320, 640, 1600, 3200, and 6400 averages), 2 K Hz (64, 128, 192, 320, 640, 1280, 3200, 6400, and 12800 averages), 3 K Hz (128, 192, 320, 640, 1280, 3200, 6400, and 12800 averages), and 4 K Hz (128, 256, 384, 640, 1280, 2650, 6400, 12800, and 25600 averages). The axial resolution for PLED-PAI is 268 μm (Fig. 3E), and there were no significant differences in lateral and axial profiles (Figs. 3C, D).

Fig. 4B, C, D, E, and F show photoacoustic images acquired using PLED-PAI for samples with 1.1 mm, 0.83 mm, 0.75 mm, 0.59 mm, and 0.55 mm line spacing, respectively. Lateral line profiles were plotted for all samples. The 550 μm spacing cannot be resolved (Fig. 4G), but the 590 μm spacing can be distinguished (10 peaks/troughs seen in data, which corresponds to the number of parallel lines scanned). Thus, the photoacoustic lateral resolution is

between 550 μm and 590 μm (Fig. 4G). Importantly, these experiments used 70 ns pulse widths. By decreasing the pulse width and having higher frequency ultrasound transducers, we could improve the lateral and axial resolutions. This work is underway. However, as we emphasized in the introduction, low spatial resolution photoacoustic data has utility in many photoacoustic sensing rather than true photoacoustic imaging.

Spatial resolution in PAI systems highly depends on laser pulse width and ultrasound transducer specification such as number of element, central frequency, and element size. Niederhauser et al. [45] measured the axial resolution of 300 μm with central frequency of 5.5 MHz for their handheld PAI system with near infrared red laser pulses (60 ns) as illumination source and detected individual blood vessels with range of 100–300 μm. Daoudi et al. [25] utilized a diode laser with pulse width of 130 ns as excitation source and 128 element with a length of 5 mm and central frequency 7.5 MHz as ultrasound detection reported 280 μm for axial resolution and wide range of 400 μm – 600 μm as lateral resolution. Kim et al. [46] calculated photoacoustic axial resolution of 400 μm for their handheld dual modality ultrasound/photoacoustic imaging system using a laser pulse of 6.5 ns and a central frequency of 5.5 MHz. Thus, we conclude that this system has spatial and axial resolution comparable to other handheld photoacoustic imaging tools.

3.3. Photoacoustic penetration depth

The ability to penetrate deep into tissue is important for many imaging applications [47]. We hypothesized that the LED-based system would have lower penetration depth because of its lower energy relative to OPO-based systems. Our goal here was to quantify the exact depth in chicken tissue. The photoacoustic images are shown Fig. 5B, C, D, E, and G, and the results illustrate that at 1.8 cm and 2.4 cm, the target (pencil lead) is recognizable for all frame rates from 30 Hz to 0.15 Hz (Fig. 5B, C). However, at 3.2 cm, the target is not detectable at 30 Hz, 15 Hz or 10 Hz (Fig. 5G), but can be seen at 3.2 cm with a frame rate of 6 Hz and lower because at lower frame rates there is more averaging, which increases contrast (Fig. 5D, E, F). Fig. 5H shows contrast versus depth. Fig. 5I, J show a photoacoustic image of a blood sample with a frame rate of 0.15 Hz at 1.5 and 2.2 cm, respectively. Fig. 5K shows contrast versus two different depths of blood sample. The blood sample is detectable when the contrast is over than 3. The highest frame rate that could detect the blood sample was 1.5 Hz and 0.6 Hz at 1.5 cm and 2.2 cm, respectively. Error bars demonstrate the standard deviation along each measurement.

There are several parameters such as excitation source, excitation wavelength, transducer specification, and imaging target that have a significant effect on photoacoustic penetration depth. Kim et al. [46] demonstrated the capability of PAI using Nd:YAG laser to Image 5.2 cm deep inside the tissue. Recently, Zhou et al. [47] showed capability of PAI to image a specific target (stable phosphorus phthalocyanine) through 11.6 cm of chicken breast. While Daoudi et al. [25] reported penetration depth of up to 1.5 cm (frame rate of 0.43 Hz, averaging were used to increase photoacoustic SNR) using diode laser in their handheld PAI setup. Here, we illustrated the capability of the PLED-PAI to detect a strong optical absorber (pencil lead) inside chicken breast up to 3.2 cm deep with a frame rate of 15 Hz.

3.4. Exogenous contrast agent in photoacoustic imaging

Exogenous contrast agents can be targeted for specific molecules or cells for preclinical and clinical applications. Photoacoustic contrast agents have significant feasibility to assist in monitoring and diagnosis of diseases [48]. We characterized the detection limit of some common small molecules used in photoacoustic imaging: ICG, MB, and DiR. These are NIR-sensitive, Food and Drug Administration (FDA)-approved contrast agents for both fluorescent and photoacoustic imaging. Various concentrations were scanned, and the detection limits were calculated at three standard deviations above baseline. Fig. 6A, E, I show MIP images of high concentrations of ICG (640 μM, 320 μM, and 160 μM), MB (6 mM, 3 mM, and 1.5 mM), and DiR (592 μM, 296 μM, and 148 μM). Fig. 6B, F, J shows the average photoacoustic intensity along all ten ROIs for each tube associated with Fig. 6A, E, I.

Fig. 6C, G, K show MIP images for the detection limit of ICG (36 μM, 18 μM, 9 μM, and DI water), MB (1.5 mM, 0.75 mM, 0.37 mM, and DI water), and DiR (136 μM, 68 μM, 34 μM, and

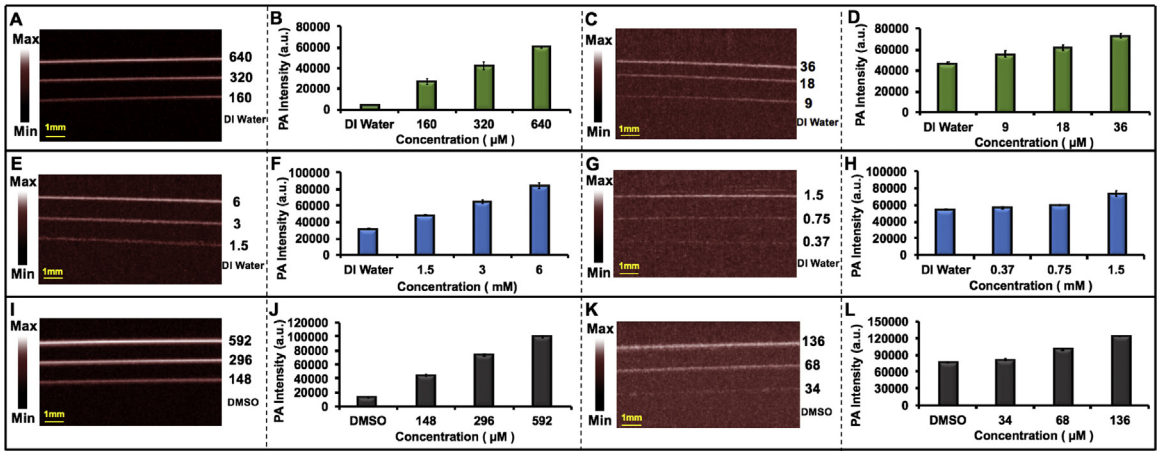

Fig. 6. Evaluation of LED-based photoacoustic imaging system for exogenous contrast agents. A) MIP image of ICG solutions (640 μM, 320 μM, 160 μM, and DI water) with high concentration as positive control inside Teflon light wall tubes. B) Statistical analysis of data in A. C) MIP image detection limit experiment for ICG (36 μM, 18 μM, 9 μM, and DI water). D) Statistical analysis of data in C. E) MIP images of MB solutions (6 mM, 3 mM, 1.5 mM, and DI water) with high concentration as positive control inside Teflon light wall tubes. F) Statistical analysis of data in E. G) MIP image detection limit experiment for MB (1.5 mM, 0.75 mM, 0.37 mM, and DI water). H) Statistical analysis of data in G. I) MIP images of DiR solutions (592 μM, 320 μM, 148 μM, and DMSO) with high concentration as positive control inside Teflon light wall tubes. J) Statistical analysis of data in I. K) MIP image detection limit experiment for DiR (136 μM, 68 μM, 34 μM, and DMSO). L) Statistical analysis of data in K. All the error bars demonstrate standard deviation between different ROIs in each tube. Scan size is 10 mm.

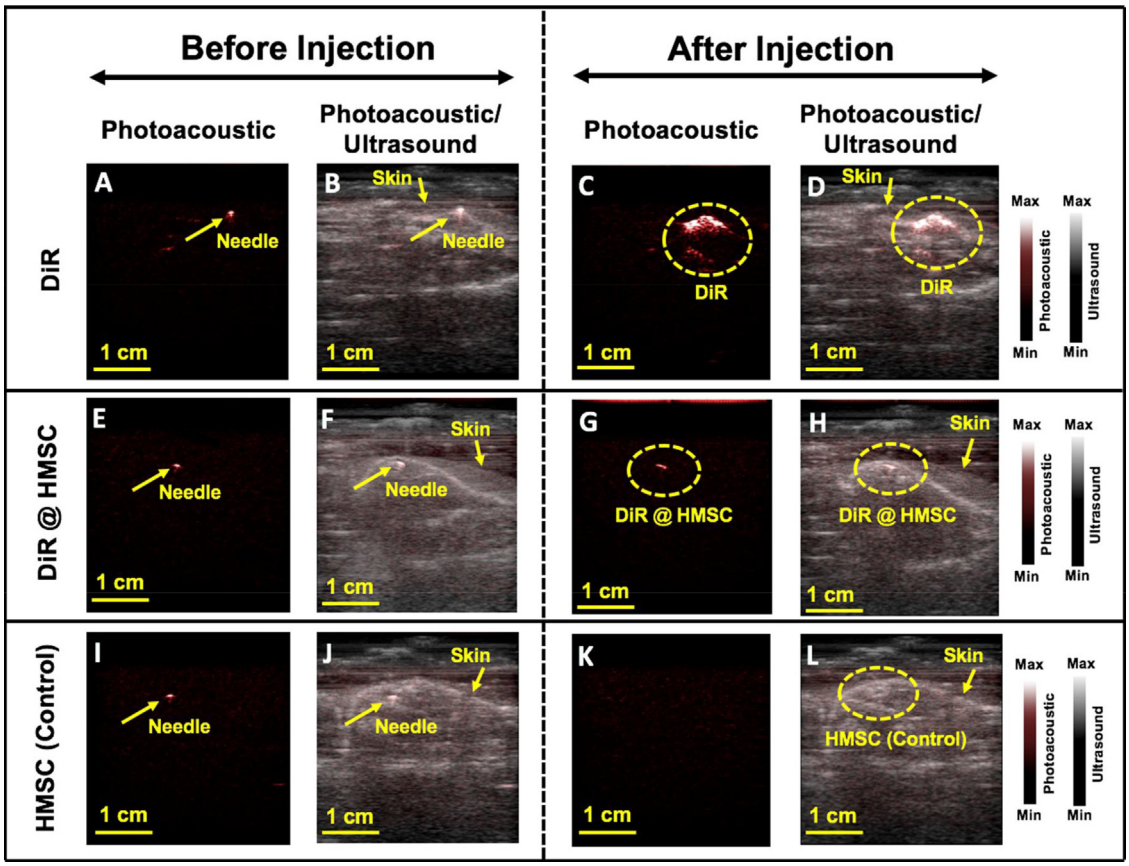

Fig. 7. *In vivo* evaluation of PLED-PAI. A) Photoacoustic image when needle is subcutaneously injected on spinal cord area before DiR injection. The needle has strong photoacoustic signal. B) Photoacoustic/ultrasound image of A. C) Photoacoustic image after subcutaneously injection of DiR. D) B-mode photoacoustic/ultrasound image of C. E) Photoacoustic image when needle is subcutaneously placed on the spinal cord area before HMSC labeled with DiR (DiR @ HMSC) injection. F) B-mode photoacoustic/ultrasound image of E. G) Photoacoustic image after injection of HMSC labeled with DiR (DiR @ HMSC) on spinal cord. H) B-mode photoacoustic/ultrasound image of G. I) Photoacoustic image in presence of needle before injection of unlabeled HMSC as control experiment. J) B-mode photoacoustic/ultrasound image of I. K) Photoacoustic image of HMSC as control. This image shows no photoacoustic signal for HMSC. L) B-mode photoacoustic/ultrasound image of K.

DMSO). Fig. 6D, H, L show the average photoacoustic intensity along the ROIs. The error bars show the standard deviation between ROIs in each tube. The limit of detection for ICG, MB, and DiR is 9 μM, 0.75 mM, and 68 μM, respectively when 850 nm is used for ICG and DiR and 690 nm is utilized for MB. The power for the LED-based system at 690 nm is almost three-fold lower than that at 850 nm. This might explain the worse detection limit for MB rather than ICG and DiR. This experiment also highlights how LED-based systems are limited by the choice of wavelength. While OPO-based systems use a tunable wavelength, this system can only use two wavelengths. Thus, it can be challenging to carefully match the absorption peak of the contrast agent with the excitation source. Nevertheless, many species absorb strongly at 690 nm or 850 nm and customized LED sets are available for ratiometric imaging.

3.5. In vivo *imaging using PLED-PAI*

After measuring and evaluating the important features such as LED beam characterization, spatial and temporal resolution, penetration depth, and capability of detection exogenous contrast agent, we next performed *in vivo* experiments to demonstrate the feasibility of PLED-PAI for clinical applications. We and others [49,50] have previously used photoacoustic imaging for stem cell imaging. Here, we used labeled cells to understand the *in vivo* performance of this LED-based system. We used DiR which has been demonstrated as an effective contrast agent for cells checking [51,52].

Fig. 7A, E, I show photoacoustic images before injection of DiR, DiR @ HMSC, and HMSC, respectively. The needle generates strong photoacoustic signal and overlaying the photoacoustic data with the ultrasound images offers more comprehensive structural information in addition to functional details from DiR-labeled cells. Fig. 7B, F, J demonstrate B-mode photoacoustic/ultrasound images before injection. Fig. 7C, D shows photoacoustic and photoacoustic/ultrasound images of injected DiR in the mice, respectively. These figures show strong photoacoustic signal in the presence of DiR. Fig. 7G shows capability of PLED-PAI to detect cells labeled with contrast agent. DiR was used as contrast agent for labeling the HMSCs. Unlabeled HMSCs were also injected as control (Fig. 7K,L), but there was no increase in photoacoustic signal. Here we demonstrated the feasibility of PLED-PAI for *in vivo* studies including photoacoustic cell imaging.

To further understand the clinical utility of the PLED-PAI, two more experiments were conducted. First, we studied a fresh enucleated rabbit eye embedded in 1% agar. Fig. 8A, B, C and D demonstrate a B-mode ultrasound image, B-mode photoacoustic/ultrasound image using 690 nm, 850 nm, and concurrent 690 and 850 nm excitation, respectively. The retinal vessels are shown with a dotted yellow Box 2 cm deep. Photoacoustic imaging of the two different wavelengths can facilitate retinal oxygen saturation measurements, but this is beyond the scope of this study. Second, PLED-PAI was utilized to image the superficial blood vessels from human volunteer wrist (Supplementary Video 1). Fig. 8E shows the

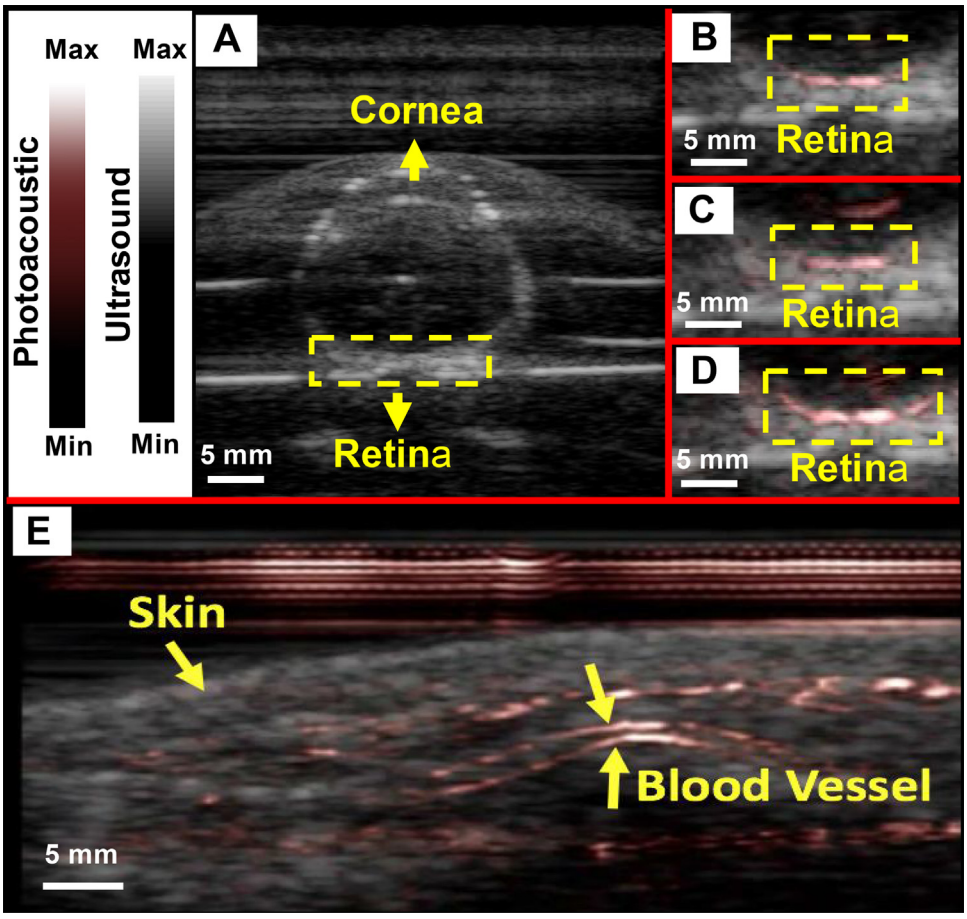

Fig. 8. Evaluation of PLED-PAI on rabbit eye. A) B-mode ultrasound image when fresh enucleated rabbit eye was embedded in 1% agar. B) B-mode photoacoustic/ultrasound image of rabbit eye using 690 nm C) B-mode Photoacoustic/ultrasound image of rabbit eye using 850 nm. D) B-mode photoacoustic/ultrasound image when both 690 and 850 nm are used at the same time. Retinal vessels are imaged in depth of 2 cm. E) Photoacoustic image of skin and vasculature. Skin and blood vessel are shown using yellow arrows. See also video in Supporting information.

photoacoustic image of human wrist. Skin and vessels are shown with yellow arrows.

4. Conclusions

In this paper, we describe a portable LED-based dual modality (ultrasound/photoacoustic) PAI system. We characterized the LED beam profile and showed that a region up to 25 mm could be imaged with a homogenous plane of light. The lateral spatial resolution was 550–590 μm, and the axial resolution was 268 μm. Temporal resolution up to 30 Hz could be achieved with penetration depths of up to 2.4 cm for pencil lead. Blood is detectable upon to 2.2 cm through chicken breast tissue with a frame rate of 0.6 Hz. We used the PLED-PAI for three well-known exogenous contrast agents (MB, ICG, and DiR) and labeled cells and showed detection limits suitable for *in vivo* imaging. We also showed the feasibility of PLED-PAI for retinal vessel monitoring.

The use of LEDs as an illumination source introduces both limitations and advantages. First, the LEDs cannot be tuned, which eliminates photoacoustic spectroscopy. Second, the pulse width of the LED was 70 ns, which affects the stress confinement satisfaction and can impact the efficiency of acoustic wave generation. Third, LEDs have low power—this can limit penetration depth at fast frame rates or temporal resolution at low frame rates. However, there are also many advantages to these systems including a significant decrease in cost, smaller footprint, lack of laser calibration and monitoring, and no need for optical goggles or light-tight shields. Thus, LED-based systems are ideal for personalized or wearable photoacoustic equipment, and we imagine that this technology could have broad utility in a number of therapeutic drug monitoring applications.

Conflict of interests

The authors declare that there is no conflict of interests regarding the publication of this paper.

Acknowledgements

Jesse V. Jokerst acknowledges funding from NIH HL117048 and HL137187 and infrastructure from S10 OD021821. The authors also thank the American Cancer Society Institutional Research (grant number 14-250-42) provided through the Moores Cancer Center, University of California, San Diego. We also knowledge UC San Diego for funding via the Frontiers of Innovation Scholars Program (FISP).

Appendix A. Supplementary data

Supplementary data associated with this article can be found, in the online version, at https://doi.org/10.1016/j.pacs.2017.11.001.

References

[1] M. Xu, L.V. Wang, Photoacoustic imaging in biomedicine, Rev. Sci. Instrum. 77 (4) (2006) 041101.
[2] L.V. Wang, Multiscale photoacoustic microscopy and computed tomography, Nat. Photonics 3 (9) (2009) 503–509.
[3] A.B. Karpiouk, B. Wang, S.Y. Emelianov, Development of a catheter for combined intravascular ultrasound and photoacoustic imaging, Rev. Sci. Instrum. 81 (1) (2010) 014901.
[4] R.G. Kolkman, P.J. Brands, W. Steenbergen, T.G. van Leeuwen, Real-time in vivo photoacoustic and ultrasound imaging, J. Biomed. Opt. 13 (5) (2008) 050510-050510-3.
[5] V. Neuschmelting, N.C. Burton, H. Lockau, A. Urich, S. Harmsen, V. Ntziachristos, M.F. Kircher, Performance of a Multispectral Optoacoustic Tomography (MSOT) System equipped with 2D vs. 3D handheld probes for potential clinical translation, Photoacoustics 4 (1) (2016) 1–10.
[6] M. Jeon, W. Song, E. Huynh, J. Kim, J. Kim, B.L. Helfield, B.Y. Leung, D.E. Goertz, G. Zheng, J. Oh, Methylene blue microbubbles as a model dual-modality contrast agent for ultrasound and activatable photoacoustic imaging, J. Biomed. Opt. 19 (1) (2014) 016005–016005.
[7] K. Pu, A.J. Shuhendler, J.V. Jokerst, J. Mei, S.S. Gambhir, Z. Bao, J. Rao, Semiconducting polymer nanoparticles as photoacoustic molecular imaging probes in living mice, Nat. Nanotechnol. 9 (3) (2014) 233–239.
[8] J. Weber, P.C. Beard, S.E. Bohndiek, Contrast agents for molecular photoacoustic imaging, Nat. Methods 13 (8) (2016) 639–650.
[9] C. Yin, X. Zhen, Q. Fan, W. Huang, K. Pu, Degradable semiconducting oligomer amphiphile for ratiometric photoacoustic imaging of hypochlorite, ACS Nano 11 (4) (2017) 4174–4182.
[10] E. Huynh, J.F. Lovell, B.L. Helfield, M. Jeon, C. Kim, D.E. Goertz, B.C. Wilson, G. Zheng, Porphyrin shell microbubbles with intrinsic ultrasound and photoacoustic properties, J. Am. Chem. Soc. 134 (40) (2012) 16464–16467.
[11] K.S. Valluru, K.E. Wilson, J.K. Willmann, Photoacoustic Imaging in oncology: translational preclinical and early clinical experience, Radiology 280 (2) (2016) 332–349.
[12] M.-L. Li, J.-T. Oh, X. Xie, G. Ku, W. Wang, C. Li, G. Lungu, G. Stoica, L.V. Wang, Simultaneous molecular and hypoxia imaging of brain tumors in vivo using spectroscopic photoacoustic tomography, Proc. IEEE 96 (3) (2008) 481–489.
[13] W. Song, Q. Wei, W. Liu, T. Liu, J. Yi, N. Sheibani, A.A. Fawzi, R.A. Linsenmeier, S. Jiao, H.F. Zhang, A combined method to quantify the retinal metabolic rate of oxygen using photoacoustic ophthalmoscopy and optical coherence tomography, Sci. Rep. 4 (2014) 6525.
[14] A. de La Zerda, Y.M. Paulus, R. Teed, S. Bodapati, Y. Dollberg, B.T. Khuri-Yakub, M.S. Blumenkranz, D.M. Moshfeghi, S.S. Gambhir, Photoacoustic ocular imaging, Opt. Lett. 35 (3) (2010) 270–272.
[15] A. Taruttis, E. Herzog, D. Razansky, V. Ntziachristos, Real-time imaging of cardiovascular dynamics and circulating gold nanorods with multispectral optoacoustic tomography, Opt. Express 18 (19) (2010) 19592–19602.
[16] L.-D. Liao, M.-L. Li, H.-Y. Lai, Y.-Y.I. Shih, Y.-C. Lo, S. Tsang, P.C.-P. Chao, C.-T. Lin, F.-S. Jaw, Y.-Y. Chen, Imaging brain hemodynamic changes during rat forepaw electrical stimulation using functional photoacoustic microscopy, Neuroimage 52 (2) (2010) 562–570.
[17] M. Nasiriavanaki, J. Xia, H. Wan, A.Q. Bauer, J.P. Culver, L.V. Wang, High-resolution photoacoustic tomography of resting-state functional connectivity in the mouse brain, Proc. Natl. Acad. Sci. 111 (1) (2014) 21–26.
[18] P.K. Upputuri, M. Pramanik, Performance characterization of low-cost, high-speed, portable pulsed laser diode photoacoustic tomography (PLD-PAT) system, Biomed. Optics Express 6 (10) (2015) 4118–4129.
[19] A. Sampathkumar, R.H. Silverman, Non-contact photoacoustic characterization of retinal vasculature for brain-injury assessment, Ultrasonics Symposium (IUS) 2014 IEEE International, IEEE, 2014, pp. 843–845.
[20] G.A. Pang, E. Bay, X. DEÁN-BEN, D. Razansky, Three-dimensional optoacoustic monitoring of lesion formation in real time during radiofrequency catheter ablation, J. Cardiovasc. Electrophysiol. 26 (3) (2015) 339–345.
[21] L. Zeng, G. Liu, D. Yang, X. Ji, Portable optical-resolution photoacoustic microscopy with a pulsed laser diode excitation, Appl. Phys. Lett. 102 (5) (2013) 053704.
[22] T. Wang, S. Nandy, H.S. Salehi, P.D. Kumavor, Q. Zhu, A low-cost photoacoustic microscopy system with a laser diode excitation, Biomed. Optics Express 5 (9) (2014) 3053–3058.
[23] T.J. Allen, P.C. Beard, Pulsed near-infrared laser diode excitation system for biomedical photoacoustic imaging, Opt. Lett. 31 (23) (2006) 3462–3464.
[24] P.K. Upputuri, M. Pramanik, Pulsed laser diode based optoacoustic imaging of biological tissues, Biomed. Phys. Eng. Express 1 (4) (2015) 045010.
[25] K. Daoudi, P. Van Den Berg, O. Rabot, A. Kohl, S. Tisserand, P. Brands, W. Steenbergen, Handheld probe integrating laser diode and ultrasound transducer array for ultrasound/photoacoustic dual modality imaging, Opt. Express 22 (21) (2014) 26365–26374.
[26] R.S. Hansen, Using high-power light emitting diodes for photoacoustic imaging, SPIE Medical Imaging, Int. Soc. Optics. Photonics (2011) 79680A-79680A-6.
[27] T.J. Allen, P.C. Beard, High power visible light emitting diodes as pulsed excitation sources for biomedical photoacoustics, Biomed. Opt. Express 7 (4) (2016) 1260–1270.
[28] Y. Adachi, T. Hoshimiya, Photoacoustic imaging with multiple-wavelength light-emitting diodes, Japanese, J. Appl. Phys. 52 (7S) (2013) (07HB06).
[29] N. Puri, Comparative study of diode laser versus neodymium-yttrium aluminum: garnet laser versus intense pulsed light for the treatment of hirsutism, J. Cutan. Aesthet. Surg. 8 (2) (2015) 97.
[30] Y. Zhang, M. Jeon, L.J. Rich, H. Hong, J. Geng, Y. Zhang, S. Shi, T.E. Barnhart, P. Alexandridis, J.D. Huizinga, Non-invasive multimodal functional imaging of the intestine with frozen micellar naphthalocyanines, Nat. Nanotechnol. 9 (8) (2014) 631–638.
[31] M.F. Kircher, A. De La Zerda, J.V. Jokerst, C.L. Zavaleta, P.J. Kempen, E. Mittra, K. Pitter, R. Huang, C. Campos, F. Habte, A brain tumor molecular imaging strategy using a new triple-modality MRI-photoacoustic-Raman nanoparticle, Nat. Med. 18 (5) (2012) 829–834.
[32] J. Wang, F. Chen, S.J. Arconada-Alvarez, J. Hartanto, L.-P. Yap, R. Park, F. Wang, I. Vorobyova, G. Dagliyan, P.S. Conti, A nanoscale tool for photoacoustic-based measurements of clotting time and therapeutic drug monitoring of heparin, Nano Lett. 16 (10) (2016) 6265–6271.
[33] K.J. Cash, C. Li, J. Xia, L.V. Wang, H.A. Clark, Optical drug monitoring: photoacoustic imaging of nanosensors to monitor therapeutic lithium in vivo, ACS nano 9 (2) (2015) 1692.
[34] P. Hai, Y. Zhou, R. Zhang, J. Ma, Y. Li, J.-Y. Shao, L.V. Wang, Label-free high-throughput detection and quantification of circulating melanoma tumor cell clusters by linear-array-based photoacoustic tomography, J. Biomed. Opt. 22 (4) (2017) 041004–041004.
[35] J.A. Viator, S. Gupta, B.S. Goldschmidt, K. Bhattacharyya, R. Kannan, R. Shukla, P. S. Dale, E. Boote, K. Katti, Gold nanoparticle mediated detection of prostate cancer cells using photoacoustic flowmetry with optical reflectance, J. Biomed. Nanotechnol. 6 (2) (2010) 187–191.
[36] C.M. O'Brien, K. Rood, S. Sengupta, S.K. Gupta, T. DeSouza, A. Cook, J.A. Viator, Detection and isolation of circulating melanoma cells using photoacoustic flowmetry, J. Vis. Exp.: JoVE 57 (2011).
[37] M.P. Mienkina, A. Eder, G. Schmitz, C.-S. Friedrich, N.C. Gerhardt, M.R. Hofmann, Simulation study of photoacoustic coded excitation using Golay codes, Ultrasonics Symposium 2008. IUS 2008. IEEE, IEEE, 2008, pp. 1242–1245.
[38] M. Sun, N. Feng, Y. Shen, X. Shen, J. Li, Photoacoustic signals denoising based on empirical mode decomposition and energy-window method, Adv. Adapt. Data Anal. 4 (01n02) (2012) 1250004.
[39] M.A.L. Bell, X. Guo, H.J. Kang, E. Boctor, Improved contrast in laser-diode-based photoacoustic images with short-lag spatial coherence beamforming, Ultrasonics Symposium (IUS) 2014 IEEE International, IEEE, 2014, pp. 37–40.
[40] S.A. Ermilov, T. Khamapirad, A. Conjusteau, M.H. Leonard, R. Lacewell, K. Mehta, T. Miller, A.A. Oraevsky, Laser optoacoustic imaging system for detection of breast cancer, J. Biomed. Opt. 14 (2) (2009) (024007-024007-14).
[41] J. Synnevag, A. Austeng, S. Holm, Adaptive beamforming applied to medical ultrasound imaging, IEEE Trans. Ultrason. Ferroelectr. Freq. Control 54 (8) (2007) 1606.
[42] K.P. Köstli, P.C. Beard, Two-dimensional photoacoustic imaging by use of Fourier-transform image reconstruction and a detector with an anisotropic response, Appl. Opt. 42 (10) (2003) 1899–1908.
[43] W. Rasband, ImageJ US National Institutes of Health, Bethesda, MD, 1997.
[44] L.V. Wang, H.-i. Wu, Biomedical Optics: Principles and Imaging, John Wiley & Sons, 2002.
[45] J.J. Niederhauser, M. Jaeger, R. Lemor, P. Weber, M. Frenz, Combined ultrasound and optoacoustic system for real-time high-contrast vascular imaging in vivo, IEEE Trans. Med. Imaging 24 (4) (2005) 436–440.
[46] C. Kim, T.N. Erpelding, L. Jankovic, M.D. Pashley, L.V. Wang, Deeply penetrating in vivo photoacoustic imaging using a clinical ultrasound array system, Biomed. Optics Express 1 (1) (2010) 278–284.
[47] Y. Zhou, D. Wang, Y. Zhang, U. Chitgupi, J. Geng, Y. Wang, Y. Zhang, T.R. Cook, J. Xia, J.F. Lovell, A phosphorus phthalocyanine formulation with intense absorbance at 1000 nm for deep optical imaging, Theranostics 6 (5) (2016) 688.
[48] G.P. Luke, D. Yeager, S.Y. Emelianov, Biomedical applications of photoacoustic imaging with exogenous contrast agents, Ann. Biomed. Eng. 40 (2) (2012) 422–437.
[49] J.V. Jokerst, M. Thangaraj, P.J. Kempen, R. Sinclair, S.S. Gambhir, Photoacoustic imaging of mesenchymal stem cells in living mice via silica-coated gold nanorods, ACS Nano 6 (7) (2012) 5920–5930.
[50] S.Y. Nam, L.M. Ricles, L.J. Suggs, S.Y. Emelianov, In vivo ultrasound and photoacoustic monitoring of mesenchymal stem cells labeled with gold nanotracers, PLoS One 7 (5) (2012) e37267.
[51] B. Zhang, X. Sun, H. Mei, Y. Wang, Z. Liao, J. Chen, Q. Zhang, Y. Hu, Z. Pang, X. Jiang, LDLR-mediated peptide-22-conjugated nanoparticles for dual-targeting therapy of brain glioma, Biomaterials 34 (36) (2013) 9171–9182.
[52] J. Huang, H. Zhang, Y. Yu, Y. Chen, D. Wang, G. Zhang, G. Zhou, J. Liu, Z. Sun, D. Sun, Biodegradable self-assembled nanoparticles of poly (d, l-lactide-co-glycolide)/hyaluronic acid block copolymers for target delivery of docetaxel to breast cancer, Biomaterials 35 (1) (2014) 550–566.

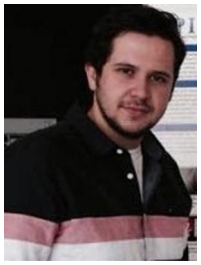

Ali Hariri is a PhD student in the Nanoengineering Department at UCSD. He got his M.S. degree and B.S degree in Biomedical Engineering from Sharif University of Technology and Amirkabir University of Technology in Iran. He worked on developing different configurations of photoacoustic imaging technique including computed tomography and microscopy (both acoustic and optical resolution). He also worked on measuring the functional connectivity in resting state using fMRI images on methamphetamine dependence.

Jeanne Lemaster is a Masters/PhD student in the Nanoengineering department at UC San Diego. She received her bachelor's degree in Chemical Engineering from The Ohio State University in Columbus, Ohio. With over 6 years of experience in research, industry, and engineering consulting, Jeanne has worked for the Department of Defense as well as the private sector on novel imaging techniques, product development, industrial design, and regulatory compliance. She is currently studying the application of nanotechnology on biosystems.

Junxin Wang is a PhD student in the Nanoengineering department at UC San Diego. He got his M.S. degree in Electro-optics from the University of Dayton and a B.S. degree in Optical Information Science and Technology from Changchun University of Science and Technology. He is currently working on biomolecular imaging using nanoparticles and extracellular vesicles.

AnanthaKrishnan Soundaram Jeevarathinam is now a Postdoctoral researcher with Dr. Jokerst Bioimaging Lab in the Nanoengineering department at the University of California, San Diego. His current research is focused on design, synthesis and study of functional organic molecular materials for bioimaging applications. Ananth received his Ph.D. from the council of scientific and industrial research – central leather research institute (CSIR-CLRI), Chennai, India.H e recently completed his postdoctoral studies with Dr. Hemali Rathnayake in the Department of Chemistry at Western Kentucky University.

Daniel L. Chao M.D., Ph.D., is an Assistant Professor of Ophthalmology at the Shiley Eye Institute. Dr. Chao earned a BS in Biomedical Engineering at Virginia Commonwealth University and an M.D. and Ph.D. in Neurosciences at Stanford University. Dr. Chao's clinical focus is in the medical and surgical treatment of retinal diseases with a special interest in macular degeneration and diabetic retinopathy. He has participated and is an active investigator in many clinical trials. He is involved in multiple interdisciplinary collaborations to develop novel imaging modalities and therapeutic approaches for retinal diseases.

Jesse Jokerst completed a B.S. cum laude at Truman State University. After a Ph.D. in Chemistry at UT Austin with John McDevitt, he completed a postdoc with Sam Gambhir in Stanford Radiology. Now an Assistant Professor in the Department of Nanoengineering at UC San Diego, the Jokerst group is eager to collaborate on projects broadly related to human health and nanotechnology.